Paper ID
DRC1030

The 3rd TSME International Conference on Mechanical Engineering
October 2012, Chiang Rai

Compliant Control of CRS Manipulator Arm

Supachock Tuntivivat, Pradya Prempraneerach*

Department of Mechanical Engineering. Rajamangala University of Technology Thanyaburi.
Pathumthani, thailand 12110
*Corresponding Author: ppradya@gmail.com, 02-549-4415

Abstract

Position and force control of a planar robot has been implemented in this research such that the end effector can follow a specified trajectory and the xy-plane force at the tip of end effector can maintain at a constant level. A compliant control uses a force sensor attached at the end effector to perform a force feedback. First the position and force controls of the end effector are designed using a mathematical model of a A255 CRS 4-axis manipulator arm in Matlab/Simulink, then these controllers are applied to a real CRS arm with motion constraint only in the vertical or xy-plane, using LabVIEW 2010. An application of this CRS arm control is to simulate a small surgery operation.
***Keywords**:* Compliant control, CRS manipulator arm, motion trajectory

1. Introduction

Both industry and medical applications move toward automated systems for various tasks. Robots, especially a manipulator arm, are one of the key components in automation; for example, pick-and-place, welding, small surgery. Main advantages of robotic arm are its precision, accuracy, and extended operational period.

Recently, researches on force control of robot manipulator arm have been implemented for various applications. Wim Witvrouw and Sean Graves and etc. [1] developed a joystick controller for operators that can sense force from robot end effector. A force sensing and control of a surgical robot were studied by Peter Kazanzides and etc. [2] such that artificial organs can be transplanted. Qinjun DU designed a minimally invasive surgical robot along with its force control, this robot can be controlled by a surgeon to perform a tumor operation with good accuracy for a small wound. Moreover, Satoshi Komada and etc. [3] has worked on a robust force control based on estimation of environment, all external disturbances; such as friction force, gravity and external force, were compensated in the controller.

This research focuses on a compliant control of A255 CRS 4-axis manipulator arm. Section 2 introduces the mathematical model and associated parameters as well as hardware component of the CRS robot arm. The dynamic simulation of the compliant control, implemented by Matlab/Simulink, is described in Section 3. The experimental results of the compliant control are performed by LabVIEW 2010 on the CRS robot arm in Section 4. Finally, Section 5 summarizes all results of the compliant control as well as states future improvement.

2. Modeling and Hardware

The A255 CRS robot arm has 5 degree of freedom as well as consists of three main linkages and 5 revolute joints. Mass and moment of inertia of all links are estimated to be $m_1 = 0.81$ kg, $m_2 = 0.52$ kg, $m_3 = 0.35$ kg, $I_1 = 0.39$ kg-m^2, $I_2 = 0.27$ kg-m^2, and $I_3 = 0.18$ kg-m^2, using the SolidWorks, as shown in Fig. 1. However, in this research the CRS robot motion is constrained with the vertical or xy-plane, only 3 links or 3 rotation angles, represented in Fig. 2, are employed for the compliant control.

The Denavit-Hartenberg parameters [1] for the CRS robot arm are given in Table 1.

Table. 1 Denavit-Hartenberg parameters of CRS robot arm

Axis	α_i	a_i	d_i	θ_i
1	0	$l_1 = 0.255$ m	0	q_1
2	0	$l_2 = 0.254$ m	0	q_2
3	0	$l_3 = 0.252$ m	0	q_3

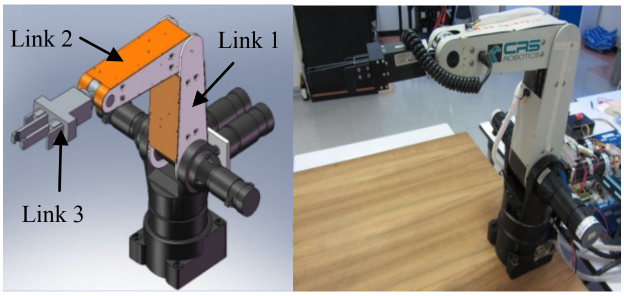

Fig. 1 All three links of the CRS arm in SolidWorks (left) and the CRS arm and its hardware (right)

where l_i is the i-th link length and t_i is the i-th rotation joint angle. According to Table 1, all α and d parameters are set to zero because the robot motion is restricted only in the vertical plane.

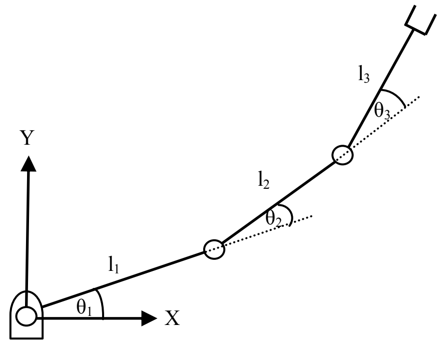

Fig. 2 Frame assignment and three degree-of-freedom of the CRS robot arm for the compliant control

A position of the CRS end effector can be calculated using a forward kinematics. The end effector position can be obtained by multiplying the following rotation matrix, given in Eq. (1), with a vector of the robot base.

$$\begin{bmatrix} c_{123} & -s_{123} & 0 & l_2*c_{12}+l_1*c_1+l_3*c_{123} \\ s_{123} & c_{123} & 0 & l_2*s_{12}+l_1*s_1+l_3*s_{123} \\ 0 & 0 & 1 & 0 \\ 0 & 0 & 0 & 1 \end{bmatrix} \quad (1)$$

Using the Lagrangian mechanics, a dynamic equation of the robot arm can be computed from total energy or Lagrangian function (L), which consists of the kinetic energy (K) and potential energy (U) in Eq. (2).

$$L = K - U \quad (2)$$

Then, the robot dynamics can be derived from the Lagrange's equation, given by the following

$$\frac{d}{dt}\left(\frac{\partial L}{\partial \dot{q}_r}\right) - \left(\frac{\partial L}{\partial q_r}\right) = Q_r \quad r = 1,2,3 \quad (3)$$

where $q_r, \dot{q}_r$ are correspondingly the r-th joint rotation angle and angular velocity. Q_r is the r-th joint torque. Vectors of the joint angle vector and angular velocity are denoted by $\mathbf{q}, \dot{\mathbf{q}}$, respectively. Finally, the robot dynamic equation can be rewritten in terms of a mass matrix ($\mathbf{M}(\mathbf{q})$), coriolis and centripetal matrix ($\mathbf{C}(\mathbf{q}, \dot{\mathbf{q}})$), gravitational matrix ($\mathbf{G}(\mathbf{q})$), and joint torque vector ($\mathbf{Q}$), as in Eq. (4) below. All matrices are described in detail in Appendix.

$$\mathbf{M}(\mathbf{q})\ddot{\mathbf{q}} + \mathbf{C}(\mathbf{q}, \dot{\mathbf{q}})\dot{\mathbf{q}} + \mathbf{G}(\mathbf{q}) = \mathbf{Q} \quad (4)$$

Three motors of the A255 CRS robot arm are driven by ASP-090-36 Accelus motor drive in a torque mode for 3-axis torque control. A NI PCI-6221 data acquisition card is interfaced between motor drives and a computer that uses LabVIEW as the control software. Two ARM7 microcontrollers are employed to count motors' encoder pulses. Fig. 3 shows the A255 CRS robot hardware connection.

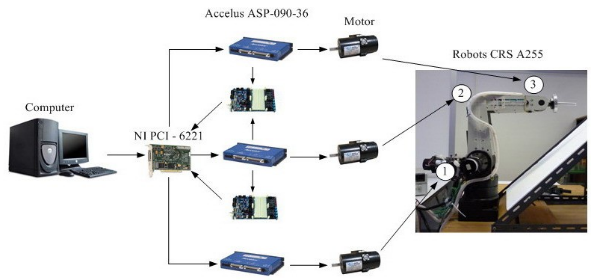

Fig. 3 Overall schematic diagram of the CRS arm hardware connection.

3. Dynamic Simulation of Compliant Control

For the force control of the CRS robot arm, a stiffness or compliant control is selected for implementation simplicity in this research. To perform the dynamic simulation of the force control, a stiffness of the contacted object (K_e) is assumed to be a constant. Thus, the normal force from the robot end effector acts on the contacted surface, is a expressed by Eq. (5).

$$f = K_e(x - x_e) \quad (5)$$

where x_e, x_c, and x_d are the equilibrium position of the contacted surface, instantaneous position of the end effector, and desired or command position of the end effector, respectively, as shown in Fig. 4.

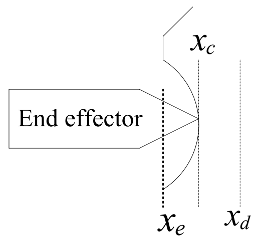

Fig. 4 Compliance of the contacted surface due to the end effector motion

A control law for the compliant control with gravity and friction compensation is given in Eq. (5) so that the normal force from the end effector can be specified.

$$\boldsymbol{\tau} = \mathbf{J}^T(\mathbf{q})(-\mathbf{K}_v\dot{x} + \mathbf{K}_p\bar{x}) + \mathbf{G}(\mathbf{q}) + \mathbf{F}(\dot{\mathbf{q}}) \quad (5)$$

where $\bar{x} = x_d - x_c$ is the position error along the perpendicular direction to the contacted surface. $\mathbf{J(q)}$ is a task-space jacobian of the end effector. A joint kinetic friction, $F(\dot{q})$, is neglected in this study. K_v and K_p are correspondingly diagonal derivative and proportional gains.

Let consider the end-effector motion along a slant or contacted surface that tilts 45 degree up from the x-axis, as shown in Fig. 5. First, a coordinate that is tangential and perpendicular to the slant surface is defined to be (u,v). Second, initial joint angles (θ_1, θ_2 θ_3) = (90°,-90°, 0°) for a CRS arm pose, displayed in Fig. 5, gives (u_i,v_i) = (0,0) or a starting location. Third, an end location is at (u_f,v_f) = (0.19,0.3). The compliant control regulates all three-motor torque such that the end effector moves from the initial position along the slant surface. Moreover, the contact forces in tangential direction (f_2) and in normal direction (f_1) are maintained at constant levels.

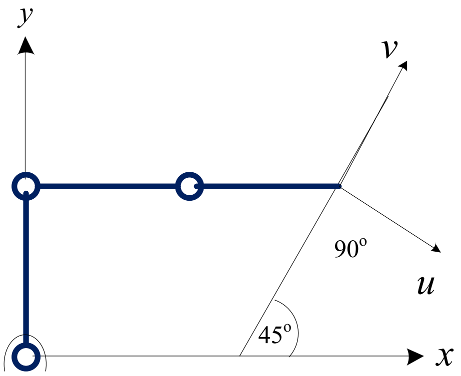

Fig. 5 Coordinate of the robot base (x,y) and of the slant surface (u,v).

Dynamic simulations of the compliant control using Eq. (4) and (5) are implemented in Matlab/Simulink. Fourth, assuming the stiffness of the contacted surface, K_e, equals to 200 N/m and tuning controller gains, (K_p, K_v) = (150,300), the CRS robot arm motion from the dynamic simulation is shown in Fig. 6. The result reveals that the controller kept the end-effector contacting with the 45° incline surface from the initial to end position very well. Three joint torques are shown in Fig. 7. The torque from the first joint varies from 2 N-m to about 0 N-m within 5 seconds during the contact operation. For the second joint, the torque maintains at a constant value of 1.98 N-m until 3 sec then decreases to 1.5 N-m.

Torque of three joints is shown in Fig. 7. The torque from the first joint varies from 2 N-m to a small value close to 0 N-m within 5 seconds during the contact operation. For the second joint, the torque maintains at a constant value of 1.98 N-m until 3 sec then decreases to 1.5 N-m. Torque in the third joint is kept constant at 0.4 N-m, which make the end effector contact the incline surface at all time. Fig. 8 displays the normal force (f1) and tangential force (f2) at the end effector. The normal force initially equals to 0 and approaches its steady state value of 0.85 N within the first 3 sec. Similarly, the tangential force increases from 0 to 0.18 N after 3 sec as well. This dynamic simulation result confirms that the end effector force can be controlled at the specified value.

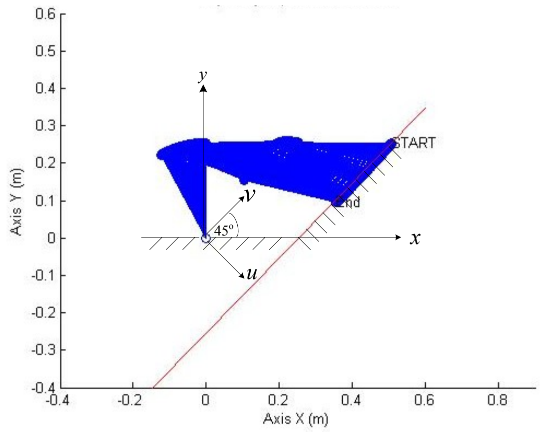

Fig. 6 Dynamic simulation of the CRS robot arm trajectory using the compliant control along the 45° incline surface.

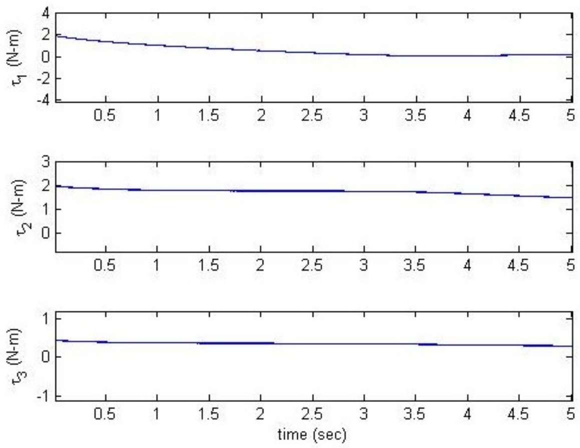

Fig. 7 Three joint torques computed from the compliant control

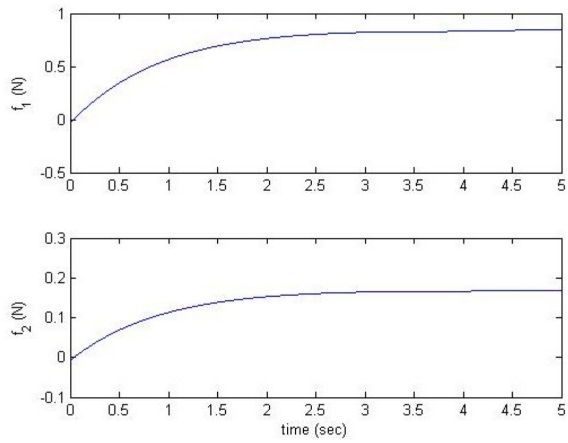

Fig. 8 Normal force (f_1) and tangential forces (f_2) of the CRS end effector exerting on the 45 incline surface

4. Experimental Results

The stiffness controller of A255 CRS robot arm is developed in LabVIEW 2010. The control law with gravity compensation in Eq. (5) is a main controller with 1) three joint angles (θ_1,θ_2,θ_3), calculated from three encoders and 2) the desired position (x_d,y_d) that is needed to transform to (u_d,v_d) in the tangential and perpendicular coordinate of the slant surface, as inputs. Outputs of the compliant controller are three joint torques, which need to convert to current commands in the form of PWM and analog signals for three Accelus drives. A simplified block diagram is shown in Fig. 9 for the compliant control of the CRS robot arm.

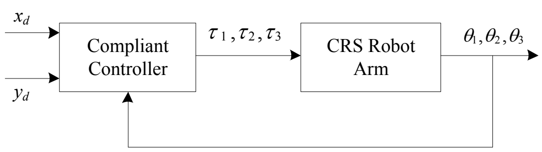

Fig. 9 Block diagram for the compliant control along with input and output for the controller

For the compliant control of the CRS robot arm along the 45° slant surface similar to the dynamic simulation, 1-inch thick foam board is used as a contacted surface on the incline plane and initial joint angles (θ_1,θ_2,θ_3) are (66°,-65°,6°). When the end effector of the CRS arm pushes and drags along the incline foam board, the joint angles, shown in Fig. 10, and joint torque, shown in Fig. 11, can be measured from motor encoders and computed from the compliant controller, respectively. According to Fig. 10, the first joint angle increases 20°, the second joint decreases 50°, and the third joint increases 35° during the compliant control operation between 2 and 2.7 sec. In the steady-state position after 3 sec, the end effector of the CRS robot arm approaches a position (u,v) = (0.184,0.3) m along the slant surface. These experimental results well agree with the dynamic simulation results, shown in Fig. 6. Note that before 2.1 sec, the CRS end effector approaches and maintains the initial position or initial joint angles using the PID position and then at 2.1 sec, the CRS arm is controlled by the compliant control. Furthermore, Fig. 11 exhibits the joint torque, computed by the compliant control. During the compliant control operation, all joint torques decrease from positive to negative values. The first joint produces the largest increment of -7 N-m at 2.1 sec, while torque difference of the second and third joints is decreased by 1.5 N-m.

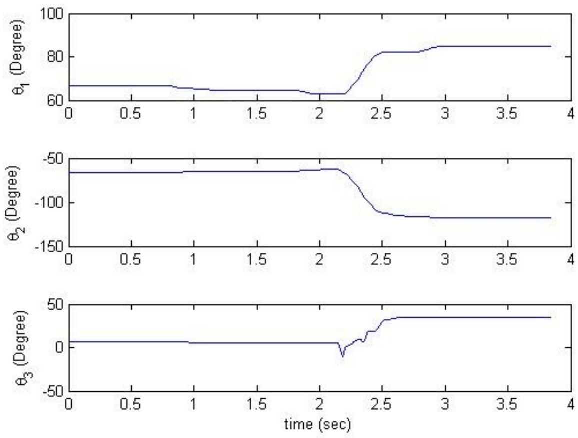

Fig. 10 Joint angles during the compliant control operation between 2.1 and 2.7 sec.

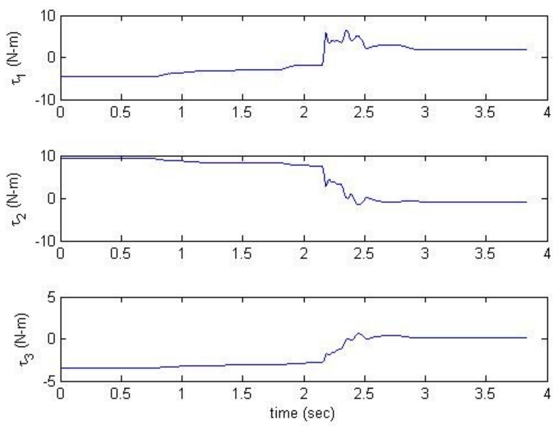

Fig. 11 Joint torques during the compliant control operation between 2.1 and 2.5 sec.

5. Conclusion

Using the compliant or stiffness controller, the A255 CRS robot arm can be controlled from the initial position (u,v) = (0,0) to the final position (u,v) = (0.19,0.3) m as well as can maintain the contacted force both in the dynamic simulation and the experimental result. However, the response in the experimental result is much faster than that in the dynamic simulation by at least 4 sec.

To further compare between dynamic simulation and experiment, the force sensor will be attached to the end effector of CRS robot arm. Moreover, different geometries of the contacted surface will be employed to demonstrate the compliant control operation of the A255 CRS robot arm.

6. Acknowledgement

The authors would like to thank the National Research Council of Thailand (NRCT) for a research grant 2553 to support this research.

7. References

[1] Craig, J.J. (1989). Introduction to robotics: mechanics and control, 2nd edition, ISBN: 0-201-09528-9, Addison-Wesley Publishing Company,

[2] Kazanzides, P., Zuhars, J., Mittelstadt, B. and Taylor, R.H. (1992). Force sensing and control for a surgical robot, paper presented in *the Proceedings of the 1992 IEEE International Conference on Robotics and Automation*, Nice, France.

[3] Wang, Q., Schutter, J.D., Witvrouw, W. and Graves, S. (1996). Derivatio of compliant motion programs based on human demonstration in *the Proceedings of the 1996 IEEE International Conference on Robotics and Automation*, Minneapolis, Minnesota.

[4] Frank, L.Lewis, Darren, M.Dawson and Chao uki, T.Abdallah. (**2003**). Robot Manipulator Control Theory And Practice, 2nd edition, ISBN: 0-8247-4072-6, CRC Press, New York.

[5] Du, Q., Huang, Q., Tian, L. and Liu, C. (**2006**). Mechanical Design and Control System of a Minimally Invasive Surgical Robot System in *the Proceedings of the **2006** IEEE International Conference on Robotics and Automation*, Luoyang, China.

[6] Komada, S., Nomura, K., Ishida, M. , Ohnishi, K. and Hori, T. (1992). Robust Force Control Based on Estimation of Environment, paper presented in *the Proceedings of the 1992 IEEE International Conference on Robotics and Automation*, Nice, France.

8. Appendix

The mass matrix ($\mathbf{M}(\mathbf{q})$) is

$$\mathbf{M} = \begin{bmatrix} M_{11} & M_{12} & M_{13} \\ M_{21} & M_{22} & M_{23} \\ M_{31} & M_{32} & M_{33} \end{bmatrix}, \text{ where}$$

$$M_{11} = I_1 + I_2 + I_3 + \left(\frac{L_1^2 m_1}{4}\right) + L_1^2 m_2 + L_1^2 m_3 + \left(\frac{L_2^2 m_2}{4}\right) + L_2^2 m_3$$
$$+ \left(\frac{L_3^2 m_3}{4}\right) + L_1 L_3 m_3 \cos(q_2 + q_3) + L_1 L_2 m_2 \cos(q_2)$$
$$+ 2L_1 L_2 m_3 \cos(q_2) + L_2 L_3 m_3 \cos(q_3)$$

$$M_{12} = I_2 + I_3 + \left(\frac{L_2^2 m_2}{4}\right) + L_2^2 m_3 + \left(\frac{L_3^2 m_3}{4}\right) + \left(\frac{L_1 L_3 m_3 \cos(q_2 + q_3)}{2}\right)$$
$$+ \left(\frac{L_1 L_2 m_2 \cos(q_2)}{2}\right) + L_1 L_2 m_3 \cos(q_2) + L_2 L_3 m_3 \cos(q_3)$$

$$M_{13} = I_3 + \left(\frac{L_3^2 m_3}{4}\right) + \left(\frac{L_1 L_3 m_3 \cos(q_2 + q_3)}{2}\right) + \left(\frac{L_2 L_3 m_3 \cos(q_3)}{2}\right)$$

$$M_{21} = I_2 + I_3\left(\frac{L_2^2 m_2}{4}\right) + L_2^2 m_3 + \left(\frac{L_3^2 m_3}{4}\right) + \left(\frac{L_1 L_3 m_3 \cos(q_2 + q_3)}{2}\right)$$
$$+ \left(\frac{L_1 L_2 m_2 \cos(q_2)}{2}\right) + L_1 L_2 m_3 \cos(q_2) + L_2 L_3 m_3 \cos(q_3)$$

$$M_{22} = I_2 + I_3\left(\frac{L_2^2 m_2}{4}\right) + L_2^2 m_3 + \left(\frac{L_3^2 m_3}{4}\right) + L_2 L_3 m_3 \cos(q_3)$$

$$M_{23} = \left(\frac{m_3 L_3^2}{4}\right) + \left(\frac{L_2 m_3 \cos(q_3) L_3}{2}\right) + I_3$$

$$M_{31} = I_3\left(\frac{L_3^2 m_3}{4}\right) + \left(\frac{L_1 L_3 m_3 \cos(q_2 + q_3)}{2}\right) + \left(\frac{L_2 L_3 m_3 \cos(q_3)}{2}\right)$$

$$M_{32} = \left(\frac{m_3 L_3^2}{4}\right) + \left(\frac{L_2 m_3 \cos(q_3)}{2}\right) + I_3$$

$$M_{33} = \left(\frac{m_3 L_3^2}{4}\right) + I_3$$

The coriolis and centripetal matrix ($\mathbf{C}(\mathbf{q}, \dot{\mathbf{q}})$) is

$$\mathbf{C} = \begin{bmatrix} C_{11} & C_{12} & C_{13} \\ C_{21} & C_{22} & C_{23} \\ C_{31} & C_{32} & C_{33} \end{bmatrix}, \text{ where}$$

$$C_{11} = \left(\frac{3L_1 L_3 m_3 (\sin(q_1 + q_3))}{2}\right) - \left(\frac{3L_1 L_2 m_2 \sin(q_1)}{2}\right) - 3L_1 L_2 m_3 \sin(q_1)$$

$$C_{12} = 0$$

$$C_{13} = \left(\frac{L_1 L_3 m_3 (\sin(q_1 + q_3))}{2}\right) - \left(\frac{L_2 L_3 m_3 \sin(q_3)}{2}\right)$$

$$C_{21} = L_1 L_2 m_3 \sin(q_2)\left(\frac{L_1 L_2 m_2 (\sin(q_1))}{2}\right) - L_1 L_2 m_3 \sin(q_1)$$
$$- \left(\frac{L_1 L_3 m_3 \sin(q_1 + q_3)}{2}\right) + \left(\frac{L_1 L_3 m_3 (\sin(q_2 + q_3))}{2}\right)$$
$$- \left(\frac{L_1 L_2 m_2 \sin(q_2)}{2}\right)$$

$$C_{22} = 0$$

$$C_{23} = \left(\frac{L_2 L_3 m_3 \sin(q_3)}{2} \right)$$

$$C_{31} = \left(\frac{L_1 L_3 m_3 (\sin(q_2 + q_3))}{2} \right) - \left(\frac{L_1 L_3 m_3 \sin(q_1 + q_3)}{2} \right)$$

$$+ \left(\frac{L_2 L_3 m_3 (\sin(q_3))}{2} \right)$$

$$C_{32} = \left(\frac{L_2 L_3 m_3 (\sin(q_3))}{2} \right)$$

$$C_{33} = 0$$

The gravitational matrix ($\mathbf{G(q)}$) is

$$\mathbf{G} = \begin{bmatrix} G_1 \\ G_2 \\ G_3 \end{bmatrix}, \text{ where}$$

$$G_1 = \left(\frac{(g * l_2 * m_2 * \cos(q_1 + q_2))}{2} \right)$$

$$+ g * l_2 * m_3 * \cos(q_1 + q_2) + \left(\frac{(g * l_1 * m_1 * \cos(q_1))}{2} \right)$$

$$+ g * l_1 * m_2 * \cos(q_1) + g * l_1 * m_3 * \cos(q_1)$$

$$+ \left(\frac{g * l_3 * m_3 * \cos(q_1 + q_2 + q_3)}{2} \right)$$

$$G_2 = \left(\frac{g * l_2 * m_2 * \cos(q_1 + q_2)}{2} \right) + g * l_2 * m_3 * \cos(q_1 + q_2)$$

$$+ \left(\frac{g * l_3 * m_3 * \cos(q_1 + q_2 + q_3)}{2} \right)$$

$$G_3 = \left(\frac{g * l_3 * m_3 * \cos(q_1 + q_2 + q_3)}{2} \right)$$

The task-space jacobian ($\mathbf{J(q)}$) is

$$\mathbf{J} = \begin{bmatrix} J_{11} & J_{12} & J_{13} \\ J_{21} & J_{22} & J_{23} \end{bmatrix}, \text{ where theta} = 45^\circ$$

$$J_{11} = - l2 * \cos(q_1 + q_2 - theta)$$

$$- l_3 * \cos(q_1 + q_2 + q_3 - theta) - l1 * \cos(q_1 - theta)$$

$$J_{12} = - l_2 * \cos(t_1 + t_2 - theta)$$

$$- l3 * \cos(t_1 + t_2 + t_3 - theta)$$

$$J_{13} = -l_3 * \cos(q_1 + q_2 + q_3 - theta)$$

$$J_{21} = - l_2 * \sin(q_1 + q_2 - theta)$$

$$- l3 * \sin(q_1 + q_2 + q_3 - theta) - l_1 * \sin(q_1 - theta)$$

$$J_{22} = - l_2 * \sin(q_1 + q_2 - theta)$$

$$- l_3 * \sin(q_1 + q_2 + q_3 - theta)$$

$$J_{23} = -l_3 * \sin(q_1 + q_2 + q_3 - theta)$$